The Astrophysical Journal, 700:232–242, 2009 July 20 doi:10.1088/0004-637X/700/1/232

EFFECTS OF ROTATION ON STANDING ACCRETION SHOCK INSTABILITY IN NONLINEAR PHASE FOR CORE-COLLAPSE SUPERNOVAE

Wakana Iwakami[1], Kei Kotake[2], Naofumi Ohnishi[3], Shoichi Yamada[1,4], and Keisuke Sawada[3]
[1] Science & Engineering, Waseda University, 3-4-1 Okubo, Shinjuku, Tokyo, 169-8555, Japan; wakana@heap.phys.waseda.ac.jp
[2] Division of Theoretical Astronomy/Center for Computational Astrophysics, National Astronomical Observatory of Japan, 2-21-1, Osawa, Mitaka, Tokyo, 181-8588, Japan
[3] Department of Aerospace Engineering, Tohoku University, 6-6-01 Aramaki-Aza-Aoba, Aoba-ku, Sendai, 980-8579, Japan
[4] Advanced Research Institute for Science and Engineering, Waseda University, 3-4-1 Okubo, Shinjuku, Tokyo, 169-8555, Japan
Received 2008 November 4; accepted 2009 May 14; published 2009 July 1

ABSTRACT

We study the effects of rotation on standing accretion shock instability (SASI) by performing three-dimensional hydrodynamics simulations. Taking into account a realistic equation of state and neutrino heating/cooling, we prepare a spherically symmetric and steady accretion flow through a standing shock wave onto a proto-neutron star (PNS). When the SASI enters the nonlinear phase, we impose uniform rotation on the flow advecting from the outer boundary of the iron core, whose specific angular momentum is assumed to agree with recent stellar evolution models. Using spherical harmonics in space and Fourier decompositions in time, we perform mode analysis of the nonspherical deformed shock wave to observe rotational effects on the SASI in the nonlinear phase. We find that rotation imposed on the axisymmetric flow does not make any spiral modes and hardly affects sloshing modes, except for steady $l = 2, m = 0$ modes. In contrast, rotation imposed on the nonaxisymmetric flow increases the amplitude of spiral modes so that some spiral flows accreting on the PNS are more clearly formed inside the shock wave than without rotation. The amplitudes of spiral modes increase significantly with rotation in the progressive direction.

Key words: hydrodynamics – instabilities – neutrinos – supernovae: general

Online-only material: color figures

1. INTRODUCTION

Core-collapse supernovae are among the most energetic explosions in the universe, catastrophically destroying massive stars. Because they are relevant to many astrophysical phenomena (e.g., formations of compact stars such as neutron stars or black holes, nucleosynthesis, neutrino, and gravitational emissions), their physics has been of wide interest to the astrophysical community. Regardless of rigorous studies on core-collapse supernovae, the explosion mechanism is still not completely understood. Except for the lower mass progenitors, spherically symmetric supernova simulations have not yet produced explosions (e.g., Liebendörfer et al. 2005; Sumiyoshi et al. 2005, and references therein). As a result of current observations revealing the aspherical nature of the explosion (e.g., Wang et al. 2002; Tanaka et al. 2007; Maeda et al. 2008), multidimensional studies and simulations of core-collapse supernovae have explored various mechanisms of asphericity, such as the roles of convection (e.g., Herant et al. 1994; Burrows et al. 1995; Janka & Mueller 1996), magnetic field and rapid rotation (e.g., Kotake et al. 2006, references therein), standing accretion shock instability (SASI; Blondin et al. 2003; Scheck et al. 2008; Blondin & Mezzacappa 2006; Ohnishi et al. 2006, 2007; Foglizzo et al. 2006; Ott et al. 2008), and g-mode oscillations of a proto-neutron star (PNS; Burrows et al. 2006).

SASI, the hydrodynamic instability of a standing shock wave, was originally studied in the context of accreting black holes (Foglizzo 2001; Houck & Chevalier 1992). The main characteristic of SASI is that lower l modes dominate the flow dynamics, where l stands for the polar index of the spherical harmonics Y_l^m. The importance of SASI to the supernova dynamics was first pointed out by Blondin et al. (2003), who demonstrated that nonradial perturbations added to a standing supernova shock wave grow exponentially with time and lead to $l = 1$ or 2 mode deformations in the linear phase, and then the sloshing motion of the shock wave induced more violent turbulent flows in the nonlinear phase. Ohnishi et al. (2006) indicated that SASI may be the key to the explosion mechanism because SASI can decrease critical neutrino luminosity for the shock revival. To date, most realistic axisymmetric two-dimensional core-collapse simulations have revealed the appearance of SASI in the initial phase of the explosion (Burrows et al. 2006; Marek & Janka 2009). Moreover, it has been suggested that such a lower mode explosion is favorable for reproducing the synthesized elements of SN1987A (Kifonidis et al. 2006) and for explaining the origins of kick (Scheck et al. 2004), spins (Blondin & Mezzacappa 2007), and magnetic fields (Endeve et al. 2008) of pulsars.

Reflecting the growing importance of SASI, the physics behind SASI in supernova cores has recently drawn much attention. Two types of mechanisms are considered: the advective-acoustic cycle (AAC) and the purely acoustic cycle (PAC). In the AAC scenario, the entropy and vorticity perturbations advected toward PNS generate a sound wave at the location of the largest velocity gradient of the stationary flow. The sound wave propagates toward the shock wave and distorts its configuration, depending on the nonradial distribution of the fluctuation pressure. The deformed shock wave induces further amplification of the entropy and vorticity perturbations (Foglizzo et al. 2007). For the PAC scenario, the standing pressure wave propagates in the circumferential direction in the region between the spherical accretion shock wave and PNS. When the postshock pressure is slightly higher than unperturbed pressure, it pushes the shock wave outward. The outward displacement of the shock wave leads to an increase of postshock pressure in the inner region, while the postshock pressure immediately behind the shock wave decreases. Thus, the amplitude of the pressure fluctuation increases further (Blondin & Mezzacappa 2006). At this time, which mechanism really works in the supernova cores is still a topic of debate.

For the past few years, the nonaxisymmetric features of SASI have been investigated with three-dimensional simulations (Blondin & Mezzacappa 2007; Iwakami et al. 2008). The modes of SASI are divided into *sloshing* and *spiral* modes. Axisymmetric $m = 0$ modes thus far studied in two-dimensional axisymmetric models (symmetric axis is z-axis) and degenerate $|m| = l$ modes (symmetric axes are x-axis, y-axis, and so on) are classified as *sloshing* modes, where m stands for the azimuthal index of the spherical harmonics Y_l^m. When we impose random perturbation or rotating flow on these axisymmetric flows, the degeneracy is broken and the rotational modes emerge. In this situation, the $+m$ modes have different amplitudes than the $-m$ modes. Such rotating nonaxisymmetric $m \neq 0$ modes are called *spiral* modes. The sloshing modes can be expressed as degenerate spiral $\pm m$ modes which have the same amplitudes as each other. The growth of spiral modes in the linear phase has been examined by simulation with a two-dimensional polar grid of a thin wedge over the entire equatorial plane (Blondin & Shaw 2007). A deformed shock wave resulting from the growth of the spiral modes produces a spiral accretion flow inside the shock wave, which transfers the angular momentum onto the PNS. A three-dimensional SASI simulation by Blondin & Mezzacappa (2007) demonstrated that the spiral mode of $m = 1$ grew dominantly and generated a strong rotational flow, continuing to develop in the nonlinear phase when random perturbations were imposed on the nonrotating or rotating progenitor. However, our previous work (Iwakami et al. 2008) revealed that the rotational flow did not develop as much for nonrotational models. An equipartition was nearly established among different m modes on a time average in the nonlinear phase. In the flow, high-entropy blobs were produced inside the shock wave. High-velocity accreting matter ran outside the blobs, and circulating flows formed inside the blobs. The high-entropy blobs repeatedly came and went during the nonlinear phase. In contrast with the outcomes of Blondin & Mezzacappa (2007), our results were similar to those obtained by the Garching group (Woosley & Janka 2005), which revealed that large bubbles of radiation formed inside the shock wave. Why these results differed so much has not yet been understood.

The SASI for the rotating progenitor model has also been studied. Blondin & Mezzacappa (2007) demonstrated that the rotation of the infalling gas helped the spiral modes of SASI to arise, and the rotation axis of the flow was roughly aligned with the spin axis of the progenitor star. Laming (2007) derived an approximate dispersion relation for oscillations of the spherical accretion shock wave, and computed growth rates for each AAC and PAC at various ratios of the radius at the shock wave to the radius at inner boundary where the pressure is constant. He concluded that the AAC dominates for non-rotating cases, while the difference in frequencies and growth rate due to rotation, in the limit of slow rotation, is caused by the addition of a PAC. Nagakura & Yamada (2008) did the numerical simulation on the equatorial plane for the rotating black hole with the outer shock wave. They also obtained the results which suggested that PAC works for their models; note, however, that the reflection point is not clear. On the other hand, Yamasaki & Foglizzo (2008) used perturbative analysis with WKB approximation for the cylindrical shock wave, and advocated that the AAC plays a prominent role in the growth of rotational SASI. Although they are divided over the problem of which mechanism to work dominantly for rotational SASI, both of them found that the growth rate of the modes rotating in the same direction as the flow was increased by rotation.

In our preliminary paper (Iwakami et al. 2009), we imposed a perturbed rotation on the spherically symmetric flow in three dimension and confirmed the linear growth of spiral modes. In the present study, we investigated the effect of rotation on SASI in the nonlinear phase. We introduced a rotation whose axis was along the z-axis into the perturbed flow in the nonlinear phase. We conducted mode analysis expanding the deformation of the shock wave with spherical harmonics in space and Fourier series in time to distinguish between $+m$ and $-m$ modes. If the features in the nonlinear phase were similar to the results of linear analysis by Laming (2007) and Yamasaki & Foglizzo (2008), it was expected that for clockwise rotation of $\omega_\phi < 0$ the $m < 0$ modes should grow much more than the $m \geqslant 0$ modes.

The organization of this paper is as follows. We describe the numerical models and formulations for mode analysis in Section 2, present the results of computations in Section 3, and make a summary and discussion of this study in Section 4.

2. METHODS OF COMPUTATION AND ANALYSIS

2.1. Numerical Models

The numerical method is exactly the same as that used in our previous paper (Iwakami et al. 2008). Employing the ZEUS-MP/2 code (Hayes et al. 2006) for the hydro solver, we solve the dynamics of an accretion flow of matter attracted by the PNS and irradiated by neutrinos emitted from the PNS. The Shen EOS (Shen et al. 1998) is implemented according to the prescription in Kotake et al. (2003). To treat the neutrino heating and cooling, we use the light bulb approximation (see Ohnishi et al. 2006, for details) in which the neutrino heating is estimated under the assumption that neutrinos are emitted isotropically from the central object with a fixed neutrino flux, and that the matter outside the PNS is optically thin. For simplicity, we consider only the interactions of electron-type neutrinos and antineutrinos. Their temperatures are constantly assumed to be the typical values in the postbounce phase (i.e., $T_{\nu_e} = 4$ MeV and $T_{\bar{\nu}_e} = 5$ MeV). The neutrino luminosity is fixed at $L_\nu = 6.0 \times 10^{52}$ erg s^{-1}. The mass of the central object is assumed to be $M_{\rm in} = 1.4\ M_\odot$, and the mass accretion rate is set to be $\dot{M} = 1\ M_\odot$ s^{-1}.

A staggered mesh in the spherical polar coordinates system is used. The mesh has 300 radial mesh points to cover $r_{\rm in} \leqslant r \leqslant r_{\rm out}$, and 30 polar and 60 azimuthal mesh points to cover the entire solid angle. Here, $r_{\rm out} = 2000$ km is the radius of the outer boundary at which the flow was supersonic, and $r_{\rm in} \sim 50$ km is the radius of the inner boundary located roughly at the neutrino sphere. This angular resolution is enough to investigate the characteristics of SASI being dominated by lower modes (see Iwakami et al. 2008, for resolution tests).

Essentially, we impose the fixed-inflow condition on the outer boundary and the free-outflow condition on the inner boundary. In the ZEUS-MP/2 code, ghost zones are spread outside the computational region. In the ghost zones, the evolution equations are not solved, but the values for the dependent variables on the ghost points are used to specify the derivative of the variables for both the boundary condition and the higher order interpolation methods (see details in Stone & Norman 1992). In this study, the density, internal energy, electron fraction, and velocity in the outer ghost boundary are

Table 1
Summary of All Models

Model	Perturbation	β_ϕ^{a}	L [cm^2 s^{-1}]$^{\mathrm{b}}$
A0	none	···	···
A1	none	0.0100	4.6×10^{15}
A2	none	0.0125	5.8×10^{15}
A3	none	0.0150	6.9×10^{15}
A4	none	0.0200	9.2×10^{15}
B0	l=1, m=0	···	···
B1	l=1, m=0	0.0100	4.6×10^{15}
B2	l=1, m=0	0.0125	5.8×10^{15}
C0	random	···	···
C1	random	0.0100	4.6×10^{15}
C2	random	0.0150	6.9×10^{15}

Notes.
[a] Parameter for rotation in Equation 4.
[b] Specific angular momentum on the equatorial plane.

substituted into the respective variables at the outer boundary, and the density, internal energy, electron fraction, v_ϕ and v_θ at the inner boundary are done into them in the inner ghost boundary, where v_ϕ and v_θ denote the ϕ and θ components of the velocity, respectively. As a special case, v_r at the points on the inner boundary is fixed with the value of the initial flow in order to obtain a steady flow at the onset of calculation, where v_r is the radial velocity. At the points on the inner ghost boundary, v_r is determined to satisfy $v_{r,0} = v_{r,1} r_1^2 / r_0^2$ ($v_{r,0} > v_{r,1}$), which means the conservation of mass flux for one-dimensional flow, where $v_{r,0}$ is the v_r at r_0 and $v_{r,1}$ is the v_r at r_1 ($r_0 < r_1$). We confirmed the influence of inner ghost boundary condition to change the relational expression to the fixed-outflow condition ($v_{r,0} = v_{r,1}$) or the fixed-initial-flow condition ($v_{r,0} < v_{r,1}$). The change of the relational expression in the ghost boundary made little difference in the essential features of the flow.

We use the spherically symmetric steady flow as the initial condition (Yamasaki & Yamada 2005). The radial distributions of various variables for the unperturbed flows are given in our previous paper (Iwakami et al. 2008). In order to induce non-spherical instability, we add radial velocity perturbation, $\delta v_r(\theta, \phi)$, to the steady spherically symmetric flow according to the following equation:

$$v_r(r, \theta, \phi) = v_r^{1D}(r)(1 + \delta v_r(\theta, \phi)), \tag{1}$$

where $v_r^{1D}(r)$ is the unperturbed radial velocity. In this study, we consider two types of perturbation: (1) an axisymmetric $l = 1, m = 0$ single-mode perturbation

$$\delta v_r(\theta, \phi) \propto \sqrt{\frac{3}{4\pi}} \cos\theta, \tag{2}$$

and (2) a nonaxisymmetric random multimode perturbation

$$\delta v_r(\theta, \phi) \propto \mathrm{r} \quad \text{and} \quad (0 \leqslant \mathrm{r} \quad \text{and} < 1), \tag{3}$$

where rand is a pseudorandom number. These perturbation amplitudes are set to be less than 1% of the unperturbed velocity.

2.2. *Introduction of Rotation*

In contrast with a spherically symmetric accretion flow, the method to construct the stationary rotational accretion flow running through the rotationally deformed shock for core-collapse supernovae has apparently not been developed thus far.

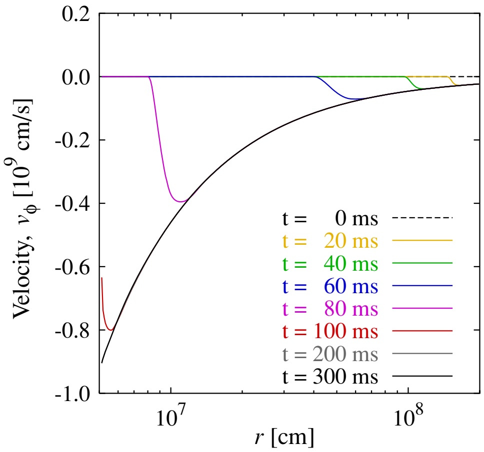

Figure 1. Radial distributions of the ϕ component of velocity along the equatorial plane ($\theta = 90°, \phi = 0°$) for Model A1. The initial flow was the steady spherically symmetric one. The rotation for $\beta_\phi = 0.01$ is imposed on the outer boundary at $t = 0$ ms. The plots of $t = 200$ ms and $t = 300$ ms overlap.

(A color version of this figure is available in the online journal.)

Hence, to investigate the effects of rotation, we impose rigid rotation on only the outer boundary. The imposed rotation is advected toward the shock wave by the accreting flow. In our preliminary work (Iwakami et al. 2009), we added the perturbed rotation to the spherically symmetric initial flow, and found the growth of spiral modes in the linear phase. However, this model of perturbed rotation generates the shock oscillation with a $l = 2, m = 0$ mode after rotational flow collides with the shock wave, and the other $m = 0$ modes grow numerically in very earlier phase just after entering the nonlinear phase. For these reasons, we consider that the above model is unsuitable for the analysis of SASI in the nonlinear phase for rotational models. So we introduce a rotational flow into the flow field in which SASI has already developed in the nonlinear phase instead of the above model. We then analyze the difference between the result with the introduction of the rotation and that without. We focus only on the nonlinear phase in this study.

We yield the rotation described as follows on the outer boundary:

$$v_\phi^{2D}(r, \theta) = v_r^{1D}(r)\beta_\phi \sin\theta, \tag{4}$$

where $v_\phi^{2D}(r, \theta)$ denotes the unperturbed ϕ component of velocity and β_ϕ denotes the rotation parameter. We examine the flow characteristics for $\beta_\phi = 0.005$–0.050, which corresponds to the specific angular momentum $L \sim (0.2\text{–}2.3) \times 10^{16}$ cm^2 s^{-1} on the equatorial plane. Table 1 lists all the models used in this study. The L of these models is chosen to be reconciled with the results of the recent presupernova calculations of rotating stars with magnetic fields by Heger et al. (2005).

Figure 1 illustrates the evolution of radial distributions of v_ϕ along the equatorial plane ($\theta = 90°, \phi = 0°$) for Model A1 by which one can see how the rotation given to the outer boundary was advected toward the PNS. At first, v_ϕ is zero everywhere when the rotational flow for $\beta_\phi = 0.01$ is introduced into the outer boundary at $t = 0$ ms. The rotational flow with v_ϕ is then advected from the outer boundary to the PNS with increasing its value by compression for $t = 20$–100 ms. At $t = 100$ ms, the rotational flow reaches the surface of the PNS, and v_ϕ hardly changes for $t = 150$–300 ms, where the plot for $t = 200$ ms overlaps with that for $t = 300$ ms.

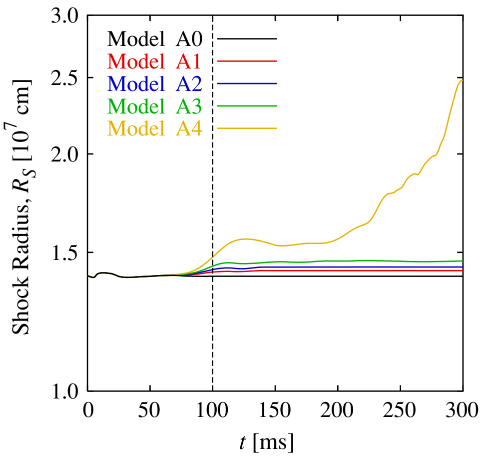

Figure 2. Time evolutions of the average shock radius R_S in the unperturbed flow for Models A0, A1, A2, A3, and A4. The time denoted by a dashed line corresponds to the time of rotation arrival at the inner boundary.

(A color version of this figure is available in the online journal.)

Figure 2 depicts the time evolutions of the average shock radius R_S for the unperturbed flow. The average shock radii for Models A0, A1, A2, and A3 are almost constant from 150 ms to 300 ms. The average shock radii for the rotating flow of Models A1, A2, and A3 are slightly larger than that for nonrotational Model A0 because of the centrifugal force. When we apply more rapid rotation like Model A4, the shock wave continues to expand outward. The models for $\beta_\phi \leqslant 0.015$ are the nonexploding models for the unperturbed flow, and allow us to analyze clearly the role of rotational SASI in flow dynamics. Thus, we focus mainly on the models for $\beta_\phi \leqslant 0.015$.

Figure 3 displays the side views of the entropy isosurfaces with the velocity vectors in the equatorial section. The entropy is expressed in the eight isosurfaces shifting from the white to the red end of the spectrum with the increasing value, and the velocity is denoted by the elongated trigonal pyramids shifting from white to blue. The hemispheres ($\pi/2 \leqslant \theta \leqslant \pi$) of eight entropy isosurfaces are superimposed on one another, and the outermost surface almost corresponds to the shock front. The central region represents the physical quantities on the spherical surface corresponding to the inner boundary. An unperturbed flow remains spherically symmetric at least until $t \sim 300$ ms (Figure 3(a)). When we introduce the clockwise rotation into the unperturbed flow at $t = 0$ ms, the rotating flow is advected inward and arrive at the inner boundary at $t \sim 100$ ms. Following that, even though the shock wave slightly oscillates, the flow remains axisymmetric at least until $t \sim 300$ ms. This result indicate that no spiral modes are generated numerically (Figure 3(b)).

2.3. *Formulation for Mode Analysis*

This section explains the mode analysis method used in this study. The deformation of the shock surface can be expanded as a linear combination of the spherical harmonics components $Y_l^m(\theta, \phi)$:

$$R_S(\theta, \phi, t) = \sum_{l=0}^{\infty} \sum_{m=-l}^{l} c_l^m(t)\, Y_l^m(\theta, \phi), \tag{5}$$

where $Y_l^m(\theta, \phi)$ is expressed by the associated Legendre polynomial $P_l^m(\cos\theta)$ and a constant K_l^m given as

$$Y_l^m(\theta, \phi) = K_l^m\, P_l^m(\cos\theta)\, e^{im\phi}, \tag{6}$$

$$K_l^m = \sqrt{\frac{2l+1}{4\pi} \frac{(l-m)!}{(l+m)!}}. \tag{7}$$

The expansion coefficients are obtained by

$$c_l^m(t) = \int_0^{2\pi} d\phi \int_0^{\pi} d\theta\, \sin\theta\, R_S(\theta, \phi, t)\, Y_l^{m*}(\theta, \phi), \tag{8}$$

where the superscript * denotes the complex conjugate. Instead of the expansion coefficients $c_l^m(t)$, we use the normalized amplitudes $c_l^m(t)/c_0^0(t)$ for the analysis.

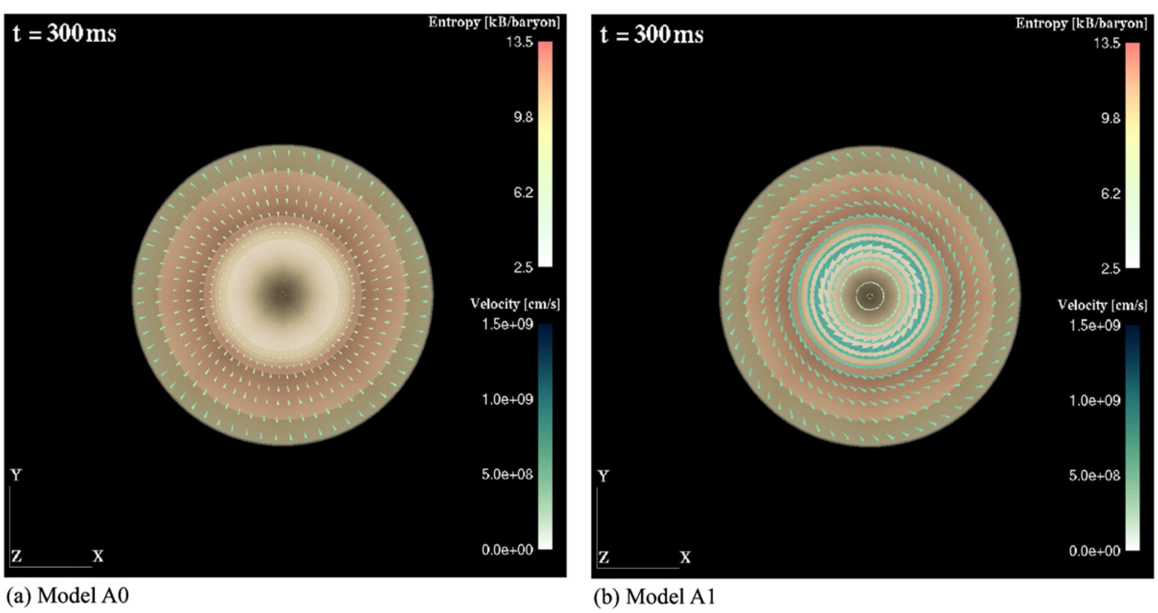

Figure 3. Entropy isosurfaces and velocity vectors in the equatorial section at $t = 300$ ms in the unperturbed flow (a) without rotation for Model A0 and (b) with rotation for Model A1. The length of each side of a panel corresponds to 5.0×10^7 cm.

(A color version of this figure is available in the online journal.)

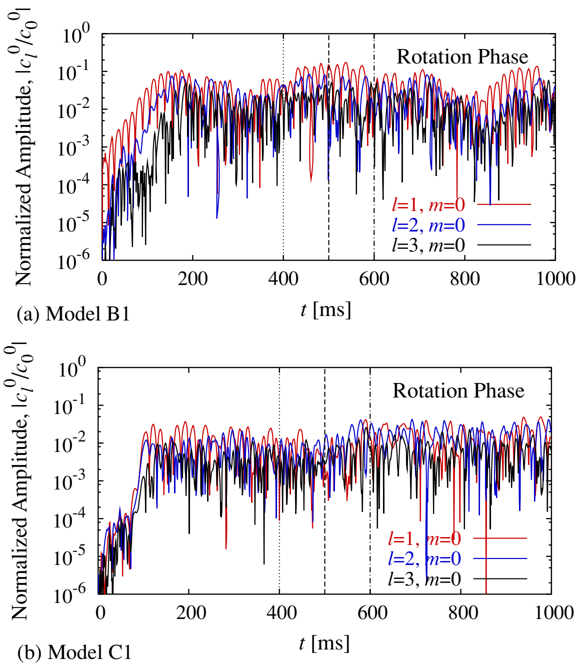

Figure 4. Time evolutions of the normalized amplitudes $|c_l^m(t)/c_0^0(t)|$. We imposed (a) axisymmetric $l = 1, m = 0$ perturbation for 2D Model B1 and (b) nonaxisymmetric random perturbation for 3D Model C1 on the spherical symmetric flow at $t = 0$ ms. The dotted line indicates the starting time to impose rotation on the outer boundary, the dashed line indicates the time of rotation arrival at the inner boundary, and the dot-dashed line indicates the onset of the rotation phase.

(A color version of this figure is available in the online journal.)

Moreover, the normalized amplitudes $c_l^m(t)/c_0^0(t)$ can be expanded to the Fourier series as follows:

$$c_l^m(t)/c_0^0(t) = \int_{-\infty}^{\infty} d\omega\, \hat{c}_l^m(\omega)\, e^{-i\omega t}, \tag{9}$$

where ω is a real number denoting an oscillation frequency. Thus, we can rewrite Equation (5) as

$$R_S(\theta, \phi, t)/c_0^0(t) = \sum_{l=0}^{\infty} \sum_{m=-l}^{l} \int_{-\infty}^{\infty} d\omega\ \hat{c}_l^m(\omega) \times K_l^m\, P_l^m(\cos\theta)\, e^{-i(\omega t - m\phi)}. \tag{10}$$

Therefore, the Fourier expansion coefficients $\hat{c}_l^m(\omega)$ are calculated as

$$\hat{c}_l^m(\omega) = \frac{1}{t_e - t_s} \int_{t_s}^{t_e} dt \int_0^{2\pi} d\phi \int_0^{\pi} d\theta\ \sin\theta \left[R_S(\theta, \phi, t)\big/c_0^0(t)\right] \times K_l^m\, P_l^m(\cos\theta)\, e^{i(\omega t - m\phi)}, \tag{11}$$

where t_s is the starting time of sampling, and t_e is the ending time. The Fourier expansion of $c_l^m(t)/c_0^0(t)$ allows $\hat{c}_l^m(\omega)$ to distinguish between $+m$ and $-m$ modes.

3. RESULTS

In this study, we introduce the rotation described above into axisymmetric (two-dimensional) and nonaxisymmetric (three-dimensional) flows in the nonlinear phase at $t = 400$ ms to observe the behavior of the flow in only the nonlinear phase. We make both two-dimensional and three-dimensional flows in the nonlinear phase with three-dimensional simulation as follows. Figure 4 presents the plots of the normalized amplitudes $|c_l^m(t)/c_0^0(t)|$ as a function of time for the two-dimensional Model B1 and three-dimensional Model C1. In the two-dimensional Model B1 (Figure 4(a)), the axisymmetric $l = 1, m = 0$ perturbation is imposed on the initial flow. As we described in our previous paper (Iwakami et al. 2008), the amplitude of the $l = 1, m = 0$ mode grows exponentially in the linear phase, and the growth of amplitudes of all axisymmetric modes is saturated in the nonlinear phase. In the three-dimensional Model C1 (Figure 4(b)), the nonaxisymmetric random perturbation is imposed on the initial flow. As we mentioned in the same paper, the amplitudes of all modes grow from the beginning, and then the flow enters the nonlinear phase. For both the two-dimensional and three-dimensional flows, we impart the rotation on the outer boundary at $t = 400$ ms (dotted line). At that time, the flow is completely in the nonlinear phase. The rotational flow is carried by an accretion flow and arrives at the inner boundary around $t = 500$ ms (dashed line). Following that, the flow inside the shock wave changes, reflecting the infalling rotational flow. We define the period from 600 ms (dot-dashed line) to 1000 ms as the rotation phase. We integrate the shock radii $R_S(\theta, \phi)$ from 600 ms to 1000 ms in Equation (11) for the Fourier expansion.

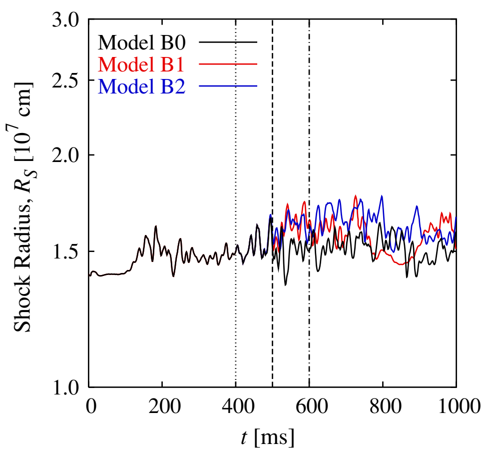

Figure 5. Time evolutions of the average shock radius R_S without rotation for Model B0 and with rotation for Models B1 and B2. The times denoted by the dotted line, dashed line, and dotted-dashed line are the same as in Figure 4.

(A color version of this figure is available in the online journal.)

3.1. Axisymmetric Rotational Model

First, we discuss the results of axisymmetric flows. All the simulations are carried out in three dimensions even for the axisymmetric flow. We dare to term the axisymmetric flow as the two-dimensional flow not to confuse the axisymmetric flow with the axisymmetric mode. When we introduce the $l = 1, m = 0$ perturbation into the nonrotational flow, only $m = 0$ modes grow, and the flow retains symmetry with respect to the z-axis even in the nonlinear phase. In other words, the sloshing modes grow, but the spiral modes do not (Iwakami et al. 2008). Confirming that only sloshing modes appear even for the rotational models, hereafter, we focus on the effect of rotation on the sloshing modes in the nonlinear phase. Furthermore, we examine that the results of the new mode analysis presented in Section 2.3 to expand the geometry of the deformed shock wave with spherical harmonics in space and Fourier transform in time, which are consistent with those of the previous mode analysis to expand with only spherical harmonics in space at the given time.

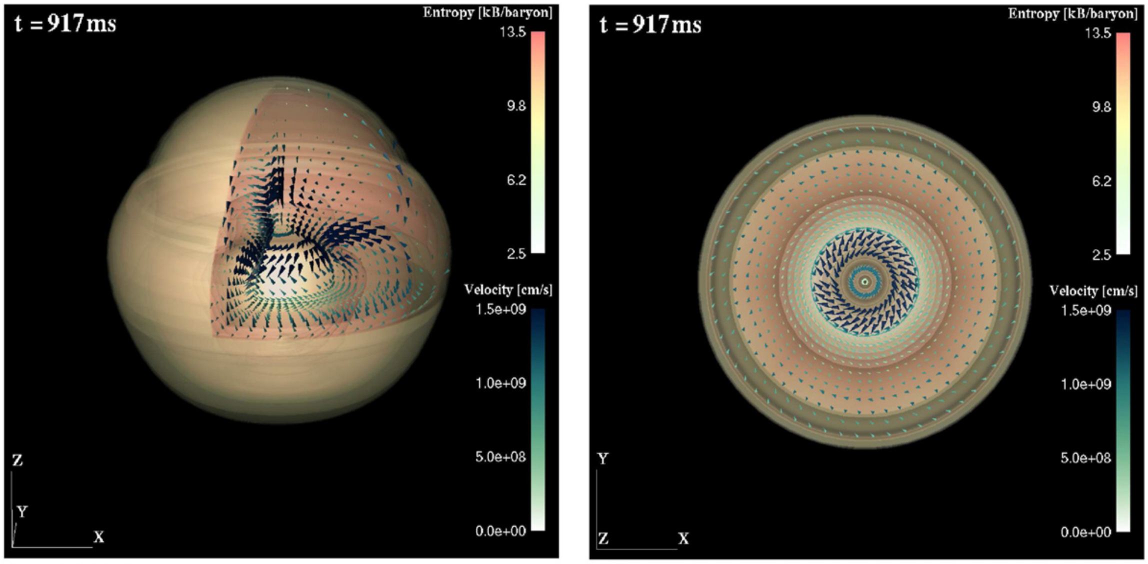

(a) Model B1 (b) Model B1

Figure 6. Partial cutaway view of the entropy isosurfaces and the velocity vectors on the cutting plane at $t = 917$ ms with rotation for Model B1. (a) The object having three cutting planes ($\theta = 90°$, $\phi = 0°$, $250°$) viewed from the side of $-y$ direction and (b) its equatorial section of $\theta = 90°$ viewed from z direction.

(A color version of this figure is available in the online journal.)

Figure 5 depicts the time evolutions of the average shock radius R_S for two-dimensional Models B0, B1, and B2. The average shock radius initially increases with the growth of SASI, and then it remains roughly constant until 500 ms with little fluctuation. After 500 ms, rotation affects the flow dynamics for Models B1 and B2. The magnitudes of average shock radii are not as different between the nonrotational Model B0 and the rotational Models B1 and B2. However, the shock wave bursts suddenly if we impose more rapid rotation on the flow. In this paper, we focus only on the nonexploding Models B1 and B2.

The flow fields for the two-dimensional rotational Model B1 are presented in Figure 6. The velocity vectors are superimposed on the cutting plane of the partial cutaway view of the entropy isosurfaces. As with the nonrotation, the flow field retains symmetry with respect to the z-axis even in the flow rotating globally (Figure 6(a)). No spiral flows form, so the flow just rotates clockwise (Figure 6(b)). Thus, it is clear that the sloshing modes grow and no spiral modes originated with numerical errors emerging.

Figure 7 presents the Fourier-transformed normalized amplitudes $|\hat{c}_l^m(\omega)|$ of $m = 0$ modes for two-dimensional Models B0, B1, and B2. The $m = 0$ modes with $\omega \neq 0$ express sloshing shock waves with oscillation frequency ω, that is, sloshing modes with ω. The steady $m = 0$ modes with $\omega = 0$ express symmetric components with respect to the z-axis of a time-averaged distortion of the shock front from $t = 600$ ms to $t = 1000$ ms estimated by Equation (11). The results of the new mode analysis indicate that the lower modes tend to be dominant, consistent with the feature obtained by the previous mode analysis presented in Figure 4(a). The magnitude of the maximum amplitudes of $l = 1$ mode and its oscillation frequency ω are almost the same between the nonrotational Model B0 and rotational Models B1 and B2. These results indicate that the rotation hardly affects the characteristics of the sloshing modes in SASI. However, the steady $l = 2, m = 0$ mode with $\omega = 0$ is much smaller for the rotational Models B1 and B2 than for the nonrotational Model B0. This may come from the fact that centrifugal force acted more strongly on the matter around the equatorial plane than near the poles. The vertically long ellipsoidal shock wave for Model B0 may be transformed into the more spherical configuration of Models B1 and B2 by rotation.

Real parts of the Fourier-transformed normalized amplitude of $l = 2, m = 0$ modes for Models B0, B1, and B2 are plotted in Figure 8. The values of the amplitudes are distinguishable between positive ones and negative ones in Figure 8, while they are not in Figure 7. The positive amplitudes of $l = 2, m = 0$ decrease with increasing rotation rates; in other words, the vertically long ellipsoidal shock wave for a nonrotational model tends to become a spherical shock wave for a rotational model. We consider that the appearance of $l = 2, m = 0$ modes for a nonrotational model might be derived from the averaged shock deformation by the nonlinear effect in the nonlinear phase. If the spherical shock wave would be transformed with harmonic oscillation, the shock wave deformation averaged during one period should be zero. On the other hand, in the case, the deformation of the shock wave deviates from the harmonic oscillations so that the averaged deformation of the shock wave might not be zero. For the axisymmetric models, the shock wave oscillates up and down along the z-axis, and is deformed to be vertically long ellipsoidal one on the average during the nonlinear phase. As the core rotates faster, the shock wave becomes more spherical one, which might be due to the centrifugal forces.

3.2. *Nonaxisymmetric Rotational Model*

Next, we consider the results of nonaxisymmetric flows. Here, we call the nonaxisymmetric flow the three-dimensional flow. When we impose a random perturbation on the nonrotational flow, both axisymmetric $m = 0$ modes and nonaxisymmetric $m \neq 0$ modes grow (Iwakami et al. 2008). In this situation, both sloshing modes and spiral modes can be generated. However, our previous mode analysis is not able to distinguish between sloshing modes and spiral modes for nonaxisymmetric $m \neq 0$ modes, because the spectra are obtained from the instantaneous deformation of the shock wave. So we use a new mode analysis in an attempt to confirm whether spiral modes are actually generated. Furthermore, we investigate the effect of rotation on sloshing and spiral modes in the nonlinear phase.

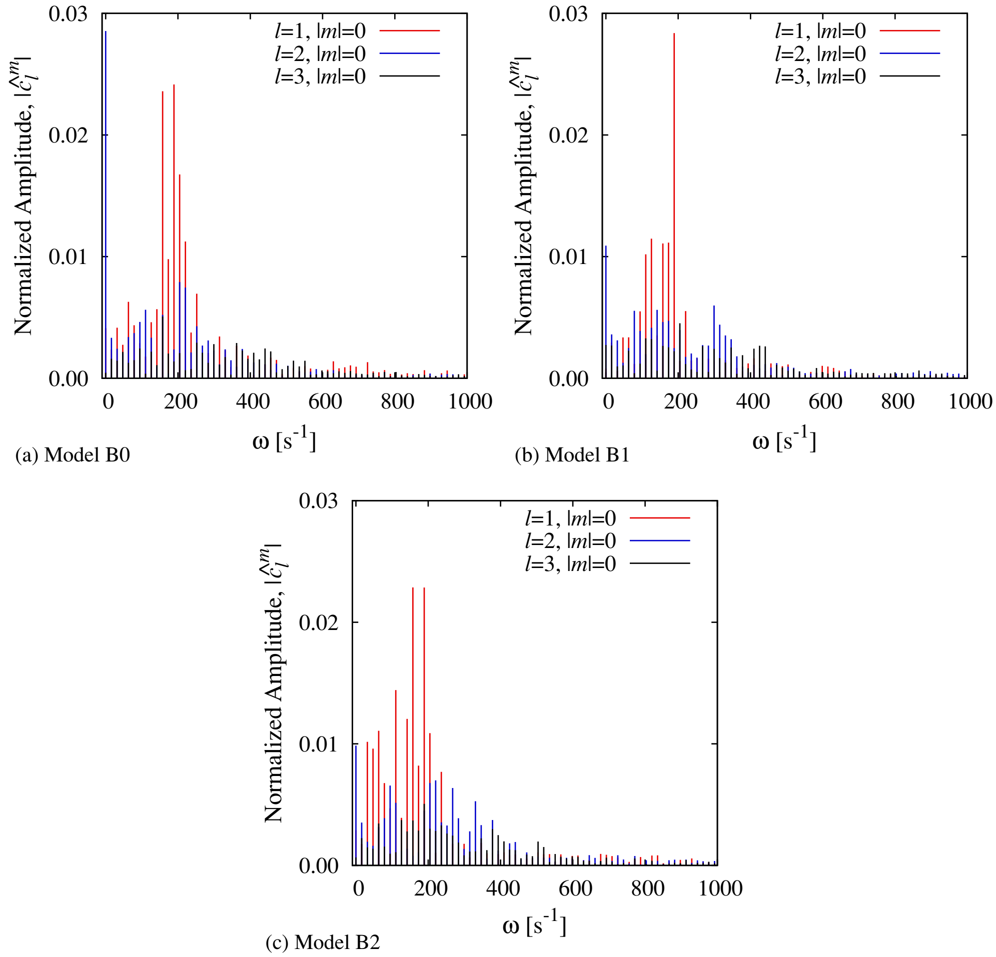

Figure 7. Fourier-transformed normalized amplitude $|\hat{c}_l^m(\omega)|$ of $m = 0$ modes without rotation for (a) Model B0 and with rotation for (b) Model B1 and (c) Model B2. Normalized amplitudes were estimated by integrating the shock deformation during the rotation phase.

(A color version of this figure is available in the online journal.)

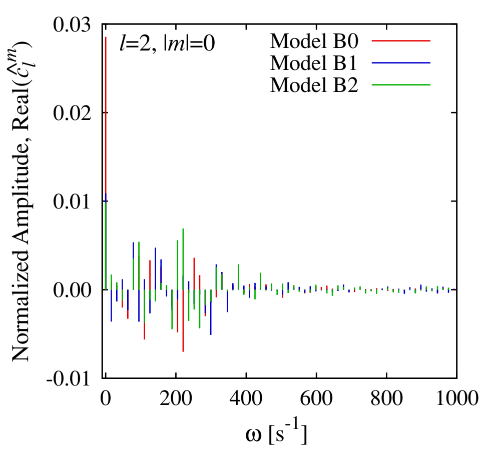

Figure 8. Real part of fourier-transformed normalized amplitude, Real ($\hat{c}_l^m(\omega)$), of $l = 2$, $|m| = 0$ modes for Model B0, B1 and B2.

(A color version of this figure is available in the online journal.)

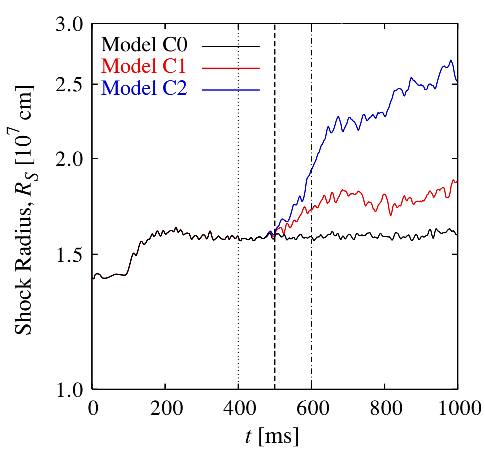

Figure 9. Time evolutions of the average shock radius R_S without rotation for Model C0 and with rotation for Models C1 and C2.

(A color version of this figure is available in the online journal.)

Figure 9 plots the average shock radius R_S as a function of time for three-dimensional Models C0, C1, and C2. As with the two-dimensional Model B0, the average shock radius increases with growing SASI from 100 ms, and then it remains nearly constant until 500 ms. At 500 ms, the flow starts to come under the influence of rotational flow falling to the PNS for Models C1 and C2. Unlike the two-dimensional models, the faster the rotation, the larger the average shock radius tends to be. When we impose more rapid rotation to the flow than in Model C2, the expansion of the shock wave continuously proceeds to the outer boundary. In this study, we therefore focus only on the nonexploding models of Models C1 and C2.

Figure 10 illustrates the flow fields for the nonrotational three-dimensional Model C0 and for the rotational three-dimensional

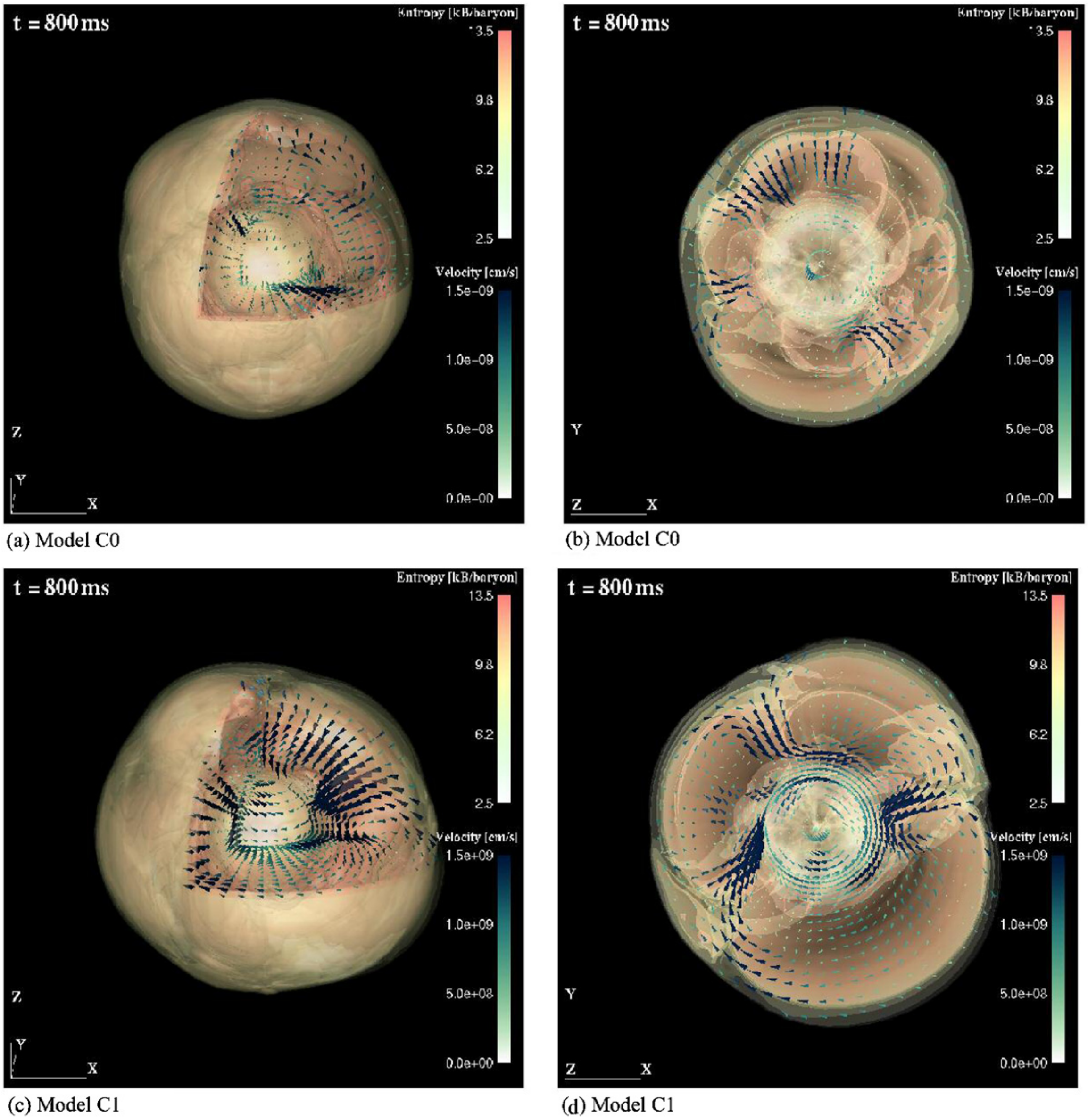

Figure 10. Partial cutaway view of the entropy isosurfaces and the velocity vectors on the cutting plane at $t = 800$ ms (a), (b) without rotation for Models C0 and (c), (d) with rotation for Model C1. One can see (a), (c) the object having three cutting planes from the $-y$ direction and (b), (d) its equatorial section from the z-direction. (A color version of this figure is available in the online journal.)

Model C1. Symmetry with respect to the z-axis is broken for both models (Figures 10(a) and (c)). Many large high-entropy blobs are observed inside the shock wave. The blobs with circulating flow arise and expand with growing SASI, and push away the shock wave outward. Matter infalling from a triple point on the shock wave runs through the interstices of the blobs with high velocity, and the stream accretes on the PNS in an arc (Figures 10(b) and (d)). A triple point is the connection point (or segment) of two shock waves propagating from both sides. When rotation is not imposed, no specific rotation axis is observed in the flow. On the other hand, as a result of introducing the rotation whose axis corresponded to the z-axis, the flow inside the shock wave rotates globally around the z-axis, and accreting spiral flows have higher velocity than that for nonrotational models because of ϕ component of velocity. After the accreting flows turn in the rotational direction near the PNS, the flows go up inside the high-entropy blobs with higher velocity than that for nonrotational models (Figure 10(d)). This is favorable for the shock expansion. Moreover, after the upward flow with high velocity turns in the rotational direction along the shock front, the centrifugal forces act on the flow so that the shock wave could be pushed away furthermore (Figure 10(d)). These flow behaviors might explain that why the average shock radii for rotational three-dimensional models tend to be larger than that for nonrotational ones (Figure 9), while the average shock radii are not different so much between rotational and nonrotational two-dimensional models (Figure 5). The flows accreting from the triple points with high velocity are developed in the θ direction for two-dimensional models (Figure 6(a)). Thus, the flows running in the rotational direction for two-dimensional rotational models do not have so much high velocity as that for three-dimensional ones (Figure 6(b)). Centrifugal forces, therefore, act less on the two-dimensional flow than the three-dimensional one so that the shock wave might hardly expand for the two-dimensional models.

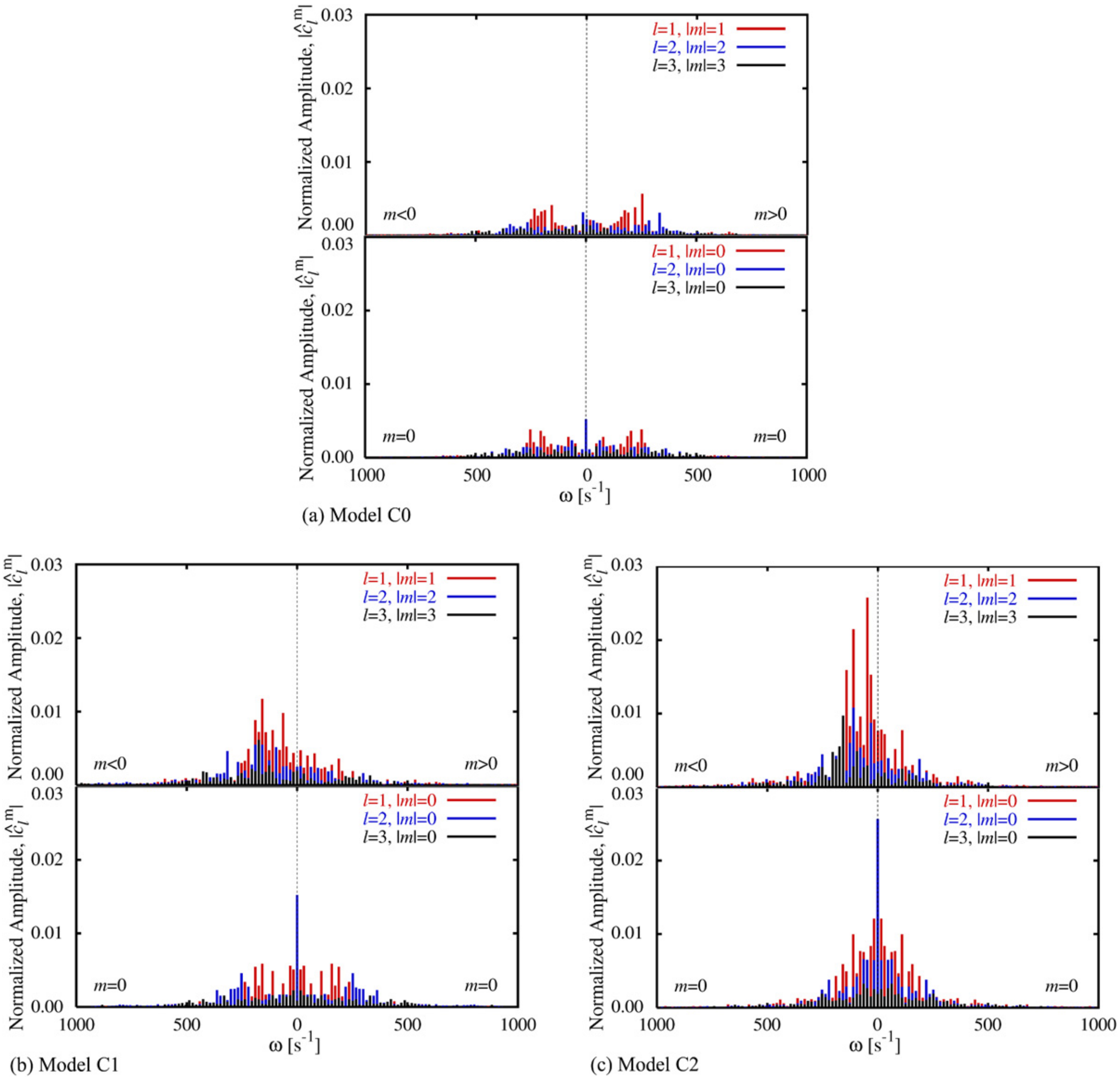

Figure 11. Fourier-transformed normalized amplitude $|\hat{c}_l^m(\omega)|$ of $m \neq 0$ and $m = 0$ modes without rotation for (a) Model C0 and with rotation for (b) Model C1 and (c) Model C2.

(A color version of this figure is available in the online journal.)

The upper panels in Figure 11 demonstrate the Fourier-transformed normalized amplitudes $|\hat{c}_l^m(\omega)|$ of $|m| = l$ modes for the three-dimensional Models C0, C1, and C2. The basis function of $|m| = l$ modes does not have any node point in the θ direction. The amplitudes of the $m > 0$ modes are plotted on the right-hand side of the graph, and those of the $m < 0$ modes are plotted on the left-hand side. The $m > 0$ modes express spiral modes rotating in the positive ϕ direction with ω, and the $m < 0$ modes express spiral modes rotating in the negative ϕ direction with ω. As a specific case, sloshing modes which are symmetric with respect to the x-axis (y-axis) could appear if $m > 0$ and $m < 0$ modes with respect to each ω for the real part (imaginary part) has equal amounts. Therefore, the mode analysis can distinguish between $m = 0$ sloshing modes and $m = l$ sloshing modes made up of equal amounts of $m > 0$ and $m < 0$ modes with ω. In this study, however, we have to mind that we use time-averaged values of mode amplitudes and absolute ones which is a square root of the sum of the square of the real part and the square of the imaginary part. If the distribution of $|\hat{c}_l^m(\omega)|$ is completely symmetric with respect to $\omega = 0$ in this figure, this result can be interpreted in three ways: (1) only sloshing $\pm m$ modes (i.e., degenerate spiral $\pm m$ modes) grow; (2) a spiral $+m$ mode and a spiral $-m$ mode emerge with the same probability; (3) both (1) and (2) occur during sampling time. On the other hand, an asymmetric distribution of $|\hat{c}_l^m(\omega)|$ suggests that the spiral m modes with a larger amplitude is dominant. Additionally, the modes with $\omega = 0$ are considered as symmetric components with respect to the x-axis or y-axis of a time-averaged distortion of the shock front from $t = 600$ ms to $t = 1000$ ms using Equation (11). The real (imaginary) part of the amplitude of $m = l$ with $\omega = 0$ describes the magnitude of the symmetric shock deformation with respect to the x-axis (y-axis). The upper panel in Figure 11(a) plots the nonrotational three-dimensional Model C0, revealing asymmetries in the distribution. We recognize that spiral modes are generated in the randomly perturbed flow even for the nonrotational model. However, the maximum amplitudes are roughly same between $m > 0$ modes and $m < 0$ modes. We assume that sloshing $\pm m$ modes dominated, or spiral $+m$ modes and spiral $-m$ modes would appear almost equal from 600 ms to 1000 ms. Figures 11(b) and (c) present the results of the rotational Models C1 and C2. The $m < 0$ modes grow more

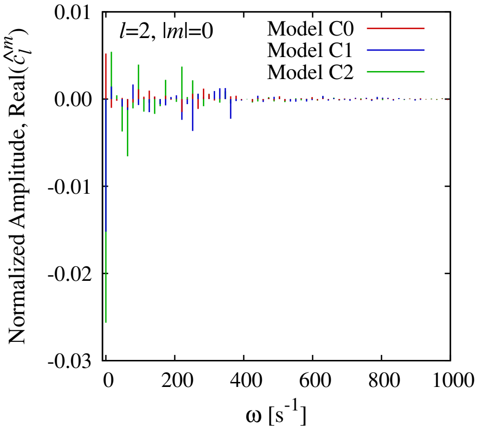

Figure 12. Real part of fourier-transformed normalized amplitude, Real ($\hat{c}_l^m(\omega)$), of $l = 2$, $|m| = 0$ modes for Models C0, C1, and C2.

(A color version of this figure is available in the online journal.)

than the $m > 0$ modes. Furthermore, the amplitude of the $m < 0$ modes becomes larger with increasing rotation. We introduce the clockwise rotation in the same direction as $m < 0$ modes. Therefore, the faster the rotation, the larger the amplitudes of the mode rotating in the same direction as a globally rotational flow tends to be.

The lower panels of Figure 11 depict the Fourier-transformed normalized amplitudes $|\hat{c}_l^m(\omega)|$ of $m = 0$ modes. The lower panel of Figure 11(a) presents the results of the nonrotational three-dimensional Model C0. Lower modes are dominant. The amplitudes for the three-dimensional Model C0 tend to be smaller than those for the two-dimensional Model B0 (Figures 7(a) and 11(a)). These results also do not conflict with those of previous mode analyses (Figures 4(a) and (b)). The lower panels of Figures 11(b) and (c) present the results of the rotational three-dimensional Models C1 and C2. The steady $l = 2, m = 0$ modes with $\omega = 0$ grew significantly. The spherical shock wave for nonrotational models might change into a horizontally long ellipsoidal one because of the centrifugal forces. The amplitudes of the sloshing modes with $\omega \neq 0$ also became somewhat large in response to the increase of rotational velocity, perhaps due to the nonlinear effects of coupling the $m = 0$ and $m \neq 0$ modes.

To compare the results of the axisymmetric models and that of the nonaxisymmetric models on the steady $l = 2, m = 0$ modes with $\omega = 0$, we present the real part of Fourier-transformed normalized amplitudes of $l = 2, m = 0$ modes for Models C0, C1, and C2 in Figure 12. The small positive amplitude of $l = 2, m = 0$ appears in the nonrotational flow for Model C0, but the negative amplitude of $l = 2, m = 0$ grows with the increasing rotation for Models C1 and C2. That is to say, the shape of the shock wave for nonrotating models, which is nearly spherical, tends to be ellipsoidal for rotating models due to the elongation along the equatorial direction. This is because of the centrifugal force acting strongly on the equatorial plane.

4. SUMMARY AND DISCUSSION

We investigated the effects of rotation on SASI in the nonlinear phase with three-dimensional hydrodynamics simulations, for the purpose of application to the supernova core in the postbounce phase. When the SASI entered the nonlinear phase, we imposed rigid rotation at the outer boundary of the iron core, whose specific angular momentum on the equatorial plane was assumed to agree with the recent stellar evolution calculations with magnetic fields. After the rotational flow arrived at the shock wave, rotation began to influence the SASI in the nonlinear phase. Focusing on this stage, we performed mode analysis for the nonspherical deformation of the shock front, using spherical harmonics in space and Fourier decompositions in time.

First, we examined the effects of rotation on SASI for the axisymmetric flow in which only sloshing modes existed before rotation was added. In the ranges of rotational strength not enough to explode, the average shock radius hardly changed with increasing angular momentum. Moreover, mode analysis revealed that the sloshing modes were also insensitive to rotation except for the $l = 2, m = 0$ mode with $\omega = 0$. Combining our results with the outcomes obtained in the linear analyses by Laming (2007) and Yamasaki & Foglizzo (2008), rotation should barely affect the growth rates of sloshing modes. The decrease of the steady $l = 2, m = 0$ modes might be a result of the centrifugal force, acting to deform the vertically long prolate configurations so that they became spherical.

Moreover, we studied the effects of rotation on SASI for the nonaxisymmetric flow in which both sloshing and spiral modes existed before rotation was added. In contrast with the axisymmetric models, the shock radius tended to expand more with increased rotation. As faster rotation was added to the flows, spiral flows ran with higher velocity from the triple points to near the PNS, and then flows circulated with higher velocity inside the high-entropy blobs. Large centrifugal force acted on the circulating flows inside the blobs, and the flows running in the rotational direction might push the shock wave further outward. As with the axisymmetric models, the effect of rotation on the $m = 0$ modes became prominent for the steady $l = 2, m = 0$ mode. The increase of the $l = 2, m = 0$ mode might be attributed to the centrifugal force which deformed the spherical shock wave to the horizontally long prolate ellipsoidal one. We observed that the other $m = 0$ modes also grew slightly with increasing rotational velocity. This result might be due to nonlinear effects of the coupling of the $m \neq 0$ modes and $m = 0$ modes. The effect of rotation on the $|m| = l$ modes became as remarked below. For nonrotational models, sloshing $\pm m$ modes were dominant, or spiral $+m$ modes and spiral $-m$ modes emerged with almost the same probability. However, for rotational models, the spiral modes rotating in the same direction as the rotational flow developed significantly with faster rotation. These results agreed with the linear analyses of SASI by Laming (2007) and Yamasaki & Foglizzo (2008).

It should be noted that the simulations highlighted in this paper are a first step toward realistic three-dimensional modeling of supernova explosions. The approximations adopted in this paper (e.g., the replacement of the PNS by the fixed inner boundary and the light-bulb approach with the constant neutrino luminosity) need improvement. It is important to clarify how rotational SASI impacts neutrino heating, but transport schemes beyond the light-bulb approaches are unquestionably needed. Confirming the outcomes of this paper will require consistent simulations in three dimensions, covering the entire stellar core and starting from gravitational collapse with better neutrino transport, which is computationally prohibitive at present. Additionally, understanding the effects of rotation on the linear growth of SASI and constructing steady accretion flows with rotation are major undertakings. The generation of pulsar spins by SASI has been addressed by Blondin & Mezzacappa (2007). Currently, we are systematically investigating a possible correlation between the kick and spin of the PNS, and our results will be presented in a forthcoming paper, along with the discussions of magnetic effect on SASI (Iwakami et al. in preparation).

W.I. expresses her sincere gratitude to K. Ueno and M. Furudate for their continuing encouragement and suggestions. K.K. is grateful to K. Sato for continuous encouragement. Numerical computations were performed on the Altix3700Bx2 at the Institute of Fluid Science, Tohoku University, as well as on XT4 and the general common use computer system at the center for Computational Astrophysics, CfCA, the National Astronomical Observatory of Japan. This study was supported in part by JSPS Research Fellowships and was partially supported by the Program for Improvement of Research Environment for Young Researchers from Special Coordination Funds for Promoting Science and Technology (SCF), the grants-in-aid for the Scientific Research (No. S19104006, No. S14102004, No. 14079202, No. 14740166, No. 20740150) and grant-in-aid for the 21st century COE program "Holistic Research and Education Center for Physics of Self-organizing Systems" of Waseda University by the Ministry of Education, Culture, Sports, Science, and Technology (MEXT) of Japan.

REFERENCES

Blondin, J. M., Mezzacappa, A., & DeMarino, C. 2003, ApJ, 584, 971
Blondin, J. M., & Mezzacappa, A. 2006, ApJ, 642, 401
Blondin, J. M., & Mezzacappa, A. 2007, Nature, 445, 58
Blondin, J. M., & Shaw, S. 2007, ApJ, 656, 366
Burrows, A., Hayes, J., & Fryxell, B. A. 1995, ApJ, 450, 830
Burrows, A., Livne, E., Dessart, L., Ott, C. D., & Murphy, J. 2006, ApJ, 640, 878
Endeve, E., Cardall, C. Y., Budiardja, R. D., & Mezzacappa, A. 2008, J. Physics Conf. Ser., 125, 012006
Foglizzo, T. 2001, A&A, 368, 311
Foglizzo, T., Scheck, L., & Janka, H.-Th. 2006, ApJ, 652, 1436
Foglizzo, T., Galletti, P., Scheck, L., & Janka, H.-Th. 2007, ApJ, 654, 1006
Hayes, J. C., Norman, M. L., Fiedler, R. A., Bordner, J. O., Li, P. S., Clark, S. E., ud-Doula, A., & Mac Low, M.-M. 2006, ApJS, 165, 188
Herant, M., Benz, W., Hix, W. R., Fryer, C. L., & Colgate, S. A. 1994, ApJ, 435, 339
Heger, A., Woosley, S. E., & Spruit, H. C. 2005, ApJ, 626, 350
Houck, J. C., & Chevalier, R. A. 1992, ApJ, 395, 592
Iwakami, W., Kotake, K., Ohnishi, N., Yamada, S., & Sawada, K. 2008, ApJ, 678, 1207
Iwakami, W., Kotake, K., Ohnishi, N., Yamada, S., & Sawada, K. 2009, Ap&SS, 322, 43
Janka, H.-Th., & Mueller, E. 1996, A&A, 306, 167
Kotake, K., Yamada, S., & Sato, K. 2003, ApJ, 595, 304
Kotake, K., Sato, K., & Takahashi, K. 2006, Rep. Prog. Phys., 69, 971
Kifonidis, K., Plewa, T., Scheck, L., Janka, H.-Th., & Müller, E. 2006, A&A, 453, 661
Laming, J. M. 2007, ApJ, 659, 1449 (erratum 687, 1461 [2008])
Liebendörfer, M., Rampp, M., Janka, H.-Th., & Mezzacappa, A. 2005, ApJ, 620, 840
Maeda, K., et al. 2008, Science, 319, 1220
Marek, A., & Janka, H.-Th. 2009, ApJ, 694, 664
Nagakura, H., & Yamada, S. 2008, ApJ, 689, 391
Ohnishi, N., Kotake, K., & Yamada, S. 2006, ApJ, 641, 1018
Ohnishi, N., Kotake, K., & Yamada, S. 2007, ApJ, 667, 375
Ott, C. D., Burrows, A., Dessart, L., & Livne, L. 2008, ApJ, 685, 1069
Scheck, L., Plewa, T., Janka, H.-Th., Kifonidis, K., & Müller, E. 2004, Phys. Rev. Lett., 92, 011103
Scheck, L., Janka, H.-Th., Foglizzo, T., & Kifonidis, K. 2008, A&A, 477, 93
Shen, H., Toki, H., Oyamatsu, K., & Sumiyoshi, K. 1998, Nucl. Phys. A, 637, 435
Stone, J. M., & Norman, M. L. 1992, ApJS, 80, 753
Sumiyoshi, K., Yamada, S., Suzuki, H., Shen, H., Chiba, S., & Toki, H. 2005, ApJ, 629, 922
Tanaka, M., Maeda, K., Mazzali, P. A., & Nomoto, K. 2007, ApJ, 668, L19
Wang, L., et al. 2002, ApJ, 579, 671
Woosley, S., & Janka, H.-Th. 2005, Nature Phys., 1, 147
Yamasaki, T., & Yamada, S. 2005, ApJ, 623, 1000
Yamasaki, T., & Foglizzo, T. 2008, ApJ, 679, 607